Real-Time Optimized Pulse Patterns to Compensate for Distorted Grid Voltages

Ellis Tsekouras, *Graduate Student Member, IEEE*, Ricardo P Aguilera, *Member, IEEE*, and Tobias Geyer, *Fellow, IEEE*

***Abstract*—For high-power converters, optimized pulse patterns (OPPs) offer excellent harmonic performance at low pulse numbers or switching frequencies. To design them, a set of nonlinear programs are typically solved offline and stored in a look-up table. An underlying limitation of precomputing OPPs is the assumption of an ideal grid voltage. In practice, voltage disturbances can emerge at a converter's point of common coupling to the grid. Consequently, precomputed OPPs are no longer optimal when the grid voltage is distorted. To overcome this limitation, a real-time OPP (RT-OPP) to compensate for a distorted grid voltage is proposed. It introduces a bilinear dynamic model of the converter's voltage harmonics with respect to switching angle adjustments. Using this, a quadratic program that can be tailored towards different objectives, such as selective harmonic control or harmonic distortion minimization, is formed. Then, an optimal analytic update policy for the switching angles is derived. To verify its performance, RT-OPP is implemented on a standard microcontroller while a grid-connected converter system is emulated on a real-time simulation platform. Experimental results demonstrate that the proposed RT-OPP algorithm can rapidly adjust a pulse pattern to compensate for a distorted grid voltage in real-time.**

***Index Terms*—Distorted grid voltage, grid-connected converters, harmonic distortion, optimized pulse patterns (OPPs), quadratic program, selective harmonic control (SHC), selective harmonic elimination (SHE).**

I. Introduction

FOR high-power converters, reducing semiconductor commutations in conjunction with lowering output current distortion is a conflicting, yet optimal objective to maximize output power [1], [2], [3]. To address this compromise, pulse patterns are an effective modulation strategy. Compared to carrier-based pulsewidth modulation (CB-PWM), the harmonic performance of pulse patterns is unparalleled at switching frequencies below 1 kHz [4]. The most popular types are selective harmonic elimination (SHE), mitigation (SHM) and optimized pulse patterns (OPPs) [5], [6], [7].

Received 22 July 2025; revised 28 September 2025 and 16 October 2025; accepted 20 October 2025. Date of publication 23 October 2025; date of current version 23 December 2025. Recommended for publication by Associate Editor H. Wu. *(Corresponding author: Ricardo P Aguilera.)*

Ellis Tsekouras and Ricardo P Aguilera are with the School of Electrical and Data Engineering, University of Technology Sydney, Broadway, NSW 2007, Australia (e-mail: ellis.tsekouras@uts.edu.au; raguilera@ieee.org).

Tobias Geyer is with ABB System Drives, 2007 Turgi, Switzerland (e-mail: t.geyer@ieee.org).

Color versions of one or more figures in this article are available at https://doi.org/10.1109/TPEL.2025.3624880.

Digital Object Identifier 10.1109/TPEL.2025.3624880

A common trait among all pulse patterns is their Fourier coefficients; these model each voltage harmonic as a function of switching angles. However, these equations are transcendental, so designing a pulse pattern is a cumbersome task. It is typically undertaken offline with the solution set stored in a look-up table (LUT). Exploring different methods for solving these equations is an ongoing area of research [8], [9], [10]. Of recent times, nonlinear programming (NLP) [11] continues to be the preferred approach [12], [13], [14], [15], [16], [17].

Since pulse patterns are computed offline, assuming nominal or ideal conditions, they are susceptible to input disturbances. This is especially relevant for grid-connected converters, as voltage distortions at their PCC to the grid are prevalent in practice [18]. Consequently, a salient challenge to advance the state-of-the-art for pulse patterns is computing them in real-time to compensate for the effect of grid voltage harmonics.

In [19], this was partially addressed by precomputing an OPP for a distorted grid voltage. An assumption of known harmonic disturbances is the key limitation. This is because grid voltage distortions or the contribution of harmonic current by neighboring converters is generally unknown [20]. Consequently, precomputing OPPs for harmonic disturbances, such as a distorted grid voltage, is ineffective [21].

The authors of this article then explored computing an OPP in real-time to compensate for estimated grid voltage harmonics [22]. This pioneering work successfully demonstrated that pulse patterns could be computed online to significantly improve harmonic performance. A limitation was the real-time OPP solver could not yield solutions at a high sample rate. Therefore, a means to adjust the OPP in between solutions is still needed. Nonetheless, it demonstrated that an OPP could be computed to compensate for a distorted grid voltage within a few hundred milliseconds.

Continuing our focus on computing pulse patterns in real-time, an artificial neural network (ANN) for selective harmonic control (SHC) has shown potential as a modulator [23]. Similar to [19] and [22], it used half-wave symmetric (HWS) pulse patterns to control a voltage harmonic's magnitude and phase. Despite exhibiting sub-millisecond execution times [24], it needs powerful research hardware to refine the pulse pattern with sequential quadratic programming (SQP).

Relying on NLP to compute pulse patterns in real-time can impact a proposal's technical feasibility. Being a cumbersome method, long execution times can limit the achievable bandwidth of a converter's grid current controller [25].

Acknowledging that a pulse pattern's transcendental Fourier coefficients are the sole culprit of their computational burden, new techniques have emerged to simplify them for expedited solving in real-time [26], [27], [28], [29]. Of these efforts, a common shortfall is their use of quarter-wave symmetric (QWS) pulse patterns. In contrast to HWS, a harmonic's phase is confined to 0^0 or $\pm 180^0$ with QWS. Considering the phase of grid voltage harmonics are diverse, QWS consequently renders a pulse pattern vulnerable to them. Furthermore, we can infer that to safeguard the harmonic performance of a pulse pattern for grid-connected converters, HWS must be assumed. Only with control of a harmonic's magnitude and phase in a pulse pattern can the effects of a distorted grid voltage be properly compensated for.

To address this challenge, a sequel to the author's preceding efforts [22] is explored in this work. The proposal is a real-time OPP (RT-OPP) to compensate for distorted grid voltages.

In contrast to the abovementioned literature, the HWS Fourier coefficients are streamlined into a bilinear dynamic model. Being linear for small switching angle adjustments, optimizing a pulse pattern can be performed with quadratic programming (QP). The distinct advantage of RT-OPP is an optimal analytic update policy to sequentially adjust switching angles with low computational burden. An agnostic formulation allows RT-OPP to be tailored toward different objectives, namely SHC and harmonic distortion minimization (HDM). The former is limited to compensating a select number of harmonics, whereas the latter minimizes a broader spectrum, like an OPP. Both objectives aim to reduce the harmonic components of the converter's output current when the grid voltage is distorted. Therefore, SHC and HDM can reduce conduction losses and improve the converter's efficiency under such conditions.

The rest of this article is organized as follows, Section II describes the formulation of HWS pulse patterns. This serves as a foundation for Section III, where RT-OPP is proposed. For completeness, three additional stages necessary to implement the proposal in real-time are also given. Section IV presents supporting experimental results for a challenging and practical case study—a converter operating with voltage distortions at its PCC to the grid. Closing remarks are then given in Section V to facilitate further exploration.

II. Half-Wave Symmetric Pulse Patterns

A. Fourier Coefficients

Pulse patterns have a modulation cycle that is of a variable length [4]. Consequently, standard carrier-based methods [3] cannot be used to synthesize them. Instead, each harmonic is modeled with respect to the switching angles

$$u_n(\boldsymbol{\alpha}, \omega t) = a_n(\boldsymbol{\alpha}) \cdot \cos(n \cdot \omega t) + b_n(\boldsymbol{\alpha}) \cdot \sin(n \cdot \omega t). \quad (1)$$

The HWS Fourier coefficients for the nth harmonic are

$$a_n(\boldsymbol{\alpha}) = \frac{-2}{n\pi} \sum_{i=1}^{2d} \Delta u_i \sin(n\alpha_i) \quad (2a)$$

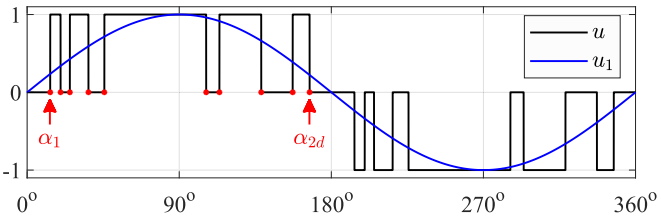

Fig. 1. HWS pulse pattern with three output voltage levels and $d = 5$ switching angles in the first quarter-cycle.

$$b_n(\boldsymbol{\alpha}) = \frac{2}{n\pi} \sum_{i=1}^{2d} \Delta u_i \cos(n\alpha_i) \quad (2b)$$

where there are $2d$ switching angles, $\boldsymbol{\alpha} = [\alpha_1 \cdots \alpha_{2d}]$, in the half-wave. An example of a HWS pulse pattern with three output voltage levels, $\Delta u_i = (-1)^{i+1}$, is shown in Fig. 1.

Solving (2) for the magnitude and phase of a single harmonic, $\vec{x_n} = a_n - jb_n$, let alone a broad spectrum, is particularly difficult for following three reasons.

1) The Fourier coefficients are formed by summing trigonometric expressions. In conjunction with their transcendental nature, nonlinear equations of this structure can lead to multiple solutions.
2) The number of switching angles sets the converter's effective switching frequency, $f_{\text{sw}} = d \cdot f_1$ Hz. This can create an overdetermined system of equations from (2) if many harmonics are modeled, $\mathcal{N}_{\text{mod}} = \text{len}([1 \cdots n \cdots N])$, such that $d < \mathcal{N}_{\text{mod}}$. A common example is an OPP, as tens or hundreds of harmonics are typically modeled with only a few switching angles [12].
3) The switching angles are constrained. For HWS Fourier coefficients, a box constraint from 0 to π must be added; $\boldsymbol{\alpha} \in [0, \pi]$. Then, to ensure they are ascending, an inequality constraint is enforced; $\alpha_i \leq \alpha_{i+1}$.

Considering their transcendental nature, a tendency for an overdetermined system, and inequality constraints on the switching angles, designing a pulse pattern using (2) is clearly a nontrivial and cumbersome task.

B. Nonlinear Programming

To this end, optimizing a pulse pattern with NLP has emerged as a consistently successful and versatile approach [17]. An example of a generalized NLP problem for a pulse pattern is given by

$$\min_{\boldsymbol{\alpha}} \quad f(\boldsymbol{\alpha}) = \sum_{n=5,7,11,\ldots}^{N} q_n \cdot \left(a_n^2 + b_n^2\right)$$

$$\text{subject to} \quad a_1 = 0, \; b_1 = m^*$$

$$\alpha_1 \leq \alpha_2 \leq \ldots \leq \alpha_{2d} \leq \pi \quad (3)$$

where m^* is the desired modulation index and q_n weights each voltage harmonic to achieve a desired harmonic objective.

Setting $q_n = 1$ with $d = \mathcal{N}_{\text{mod}}$ will uniformly penalize the modeled voltage harmonics for an exactly determined system –

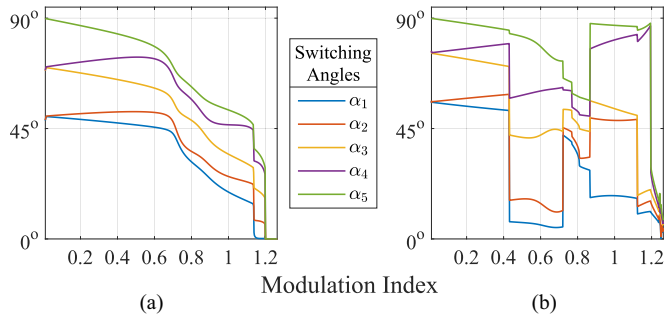

Fig. 2. Precomputed switching angles with respect to the modulation index for storage in a LUT. (a) SHE. (b) OPP.

solving this NLP will lead to an SHE pattern. To instead yield an OPP that minimizes the current total harmonic distortion (THDi) for an inductive output filter [4], one can set $q_n = 1/n^2$ and $d << \mathcal{N}_{\text{mod}}$. Adding inequality constraints on individual voltage or currents harmonics for conformance to grid-code limits, such as IEEE-519 [30], would lead to an SHM pattern.

Assuming the pulse pattern is applied by a three-phase converter, all line-to-neutral triplen harmonics are respectively eliminated in the line-to-line quantities. In addition, there are no even harmonics since odd-symmetry is imposed. Therefore, only the non-triplen odd (NTO) harmonics are modeled in (3).

C. Offline Computation and LUTs

Despite NLP being an effective approach to design pulse patterns, it has significant computational burden. Therefore, optimizing a pulse pattern is typically undertaken offline. The switching angles are precomputed for a set of modulation indexes, $m^* \in (0, 4/\pi]$, and stored in a LUT.

During converter operation, these switching angles are then recalled from the LUT to reconstruct the pulse pattern in real-time. An example of an SHE and OPP LUT for $d = 5$ with QWS are shown in Fig. 2.

To precompute pulse patterns, nominal operating conditions are typically assumed – namely, an ideal grid voltage. In practice, this approach can lead to poor harmonic performance since the grid voltage is distorted. Consequently, a converter operating with nominal pulse patterns from a LUT is susceptible to grid voltage harmonics. Overcoming this limitation is the key motivation of this work.

D. Precomputing Pulse Patterns for a Distorted Grid Voltage

To compute a pulse pattern that compensates for grid voltage distortions, the Fourier coefficient terms from (3) are updated to include them. This yields the following NLP problem:

$$\min_{\boldsymbol{\alpha}} \quad f(\boldsymbol{\alpha}) = \sum_{n=5,7,11,\ldots}^{N} q_n \cdot \left(\Delta a_n^2 + \Delta b_n^2\right)$$
$$\text{subject to} \quad a_1 = 0,\ b_1 = m^*$$
$$\alpha_1 \leq \alpha_2 \leq \ldots \leq \alpha_{2d} \leq \pi \tag{4}$$

where $\Delta a_n = a_n - a_{g;n}$ and $\Delta b_n = b_n - b_{g;n}$ encapsulate the difference in Fourier coefficients of the pulse pattern and grid voltage. If $\Delta a_n = \Delta b_n = 0$, the converter will match the magnitude and phase of the nth grid voltage harmonic. Under this condition, there is no voltage drop across the converter's output filter and this component is thereby eliminated from its output current.

A key observation is the objective function in (4) varies with the Fourier coefficients of the grid voltage harmonics, $a_{g;n}$ and $b_{g;n}$. Therefore, the optimal solution, $\boldsymbol{\alpha}^{\text{opt}}$, to (4) is unique and a new LUT is required for each case of grid voltage distortions. As a consequence, the overall size of this LUT grows exponentially with respect to the $\mathcal{N}_{\text{mod}} - 1$ grid voltage harmonics it compensates for.

The number of bytes required to store a LUT of HWS pulse patterns to compensate for a distorted grid voltage is

$$N_{\text{bytes}}^{\text{LUT}} = 2d \cdot N_{\text{bytes}}^{\alpha_i} \cdot N_m \cdot \left(N_{\text{mag}}^{v_g} \cdot N_{\phi}^{v_g}\right)^{\mathcal{N}_{\text{mod}}-1} \tag{5}$$

where $N_{\text{bytes}}^{\alpha_i}$ is the number of bytes used to store a single switching angle and N_m is the number of modulation index entries. $N_{\text{mag}}^{v_g}$ and $N_{\phi}^{v_g}$ denote the number of entries for the magnitude and phase of each grid voltage harmonic. To investigate whether it is feasible to store such a LUT, an example evaluation of (5) will be given.

Storing a switching angle as an unsigned 8-bit integer in 8Q2.6 notation occupies one byte, $N_{\text{bytes}}^{\alpha} = 1$, and yields a resolution of 0.895° for $\alpha_i \in [0, \pi)$. Assuming this is sufficient for accurate linear interpolation between entries, a HWS pulse pattern with $d = 5$ then consumes ten bytes of memory. For the modulation index, a resolution of 0.01 yields $N_m = 127$ entries for $m^* \in (0, 1.27]$. For the magnitudes of a grid voltage harmonic, a resolution of 0.01 pu yields $N_{\text{mag}}^{v_g} = 10$ for $|\vec{v}_g| \in (0, 0.1]$ p · u. whereas for the phase, a resolution of 1° yields $N_{\phi}^{v_g} = 360$ for $\arg(\vec{v}_g) \in (0°, 360°]$. To then compensate for the 5th and 7th grid voltage harmonics, $\mathcal{N}_{\text{mod}} = 3$.

Substituting these values into (5), the number of bytes required to store this LUT exceeds 16 GB – far beyond the external memory capabilities of any microcontroller. Clearly, precomputing pulse patterns for grid voltage distortions and storing them in a LUT demands significant memory. In addition, the LUT's size will grow exponentially with respect to the $\mathcal{N}_{\text{mod}} - 1$ grid voltage harmonics it compensates for.

As proposed in [23], an ANN can reduce the LUT memory to a more feasible size. However, this comes at the expense of increased computational burden, since an SQP must be solved to refine the ANN's result. Compared to an NLP approach, this work proposes to optimize a pulse pattern in real-time by solving a QP.

III. Real-Time Optimized Pulse Patterns

For completeness, the three supporting stages to implement the proposal in real-time will first be given. Then, RT-OPP is described as a QP that is constructed from a bilinear dynamic model of a pulse pattern's Fourier Coefficients. The algorithm to efficiently solve this QP is then given. Following this, design guidelines for RT-OPP is supported with numerical results.

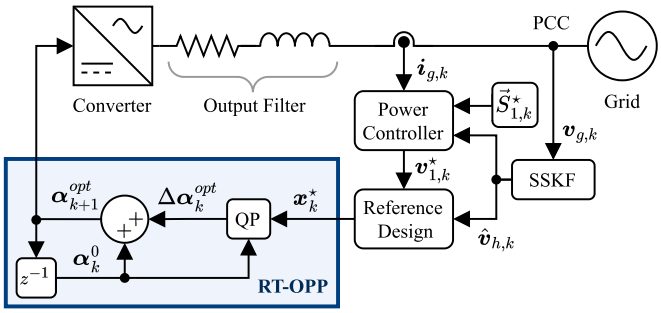

Fig. 3. Block diagram of the proposed RT-OPP with the three supporting stages to compensate for a distorted grid voltage in real-time.

A block diagram of how the proposed RT-OPP interfaces with the three supporting stages is illustrated in Fig. 3. Each stage is summarized as follows.

1) A steady-state Kalman filter (SSKF) estimates the voltage harmonics, $\hat{\boldsymbol{v}}_{h,k}$, at the converter's PCC to the grid.
2) A power controller generates the fundamental input voltage setpoint, $\boldsymbol{v}^{*}_{1,k}$, to track a fundamental apparent power setpoint, $\vec{S}^{*}_{1,k} = P^{*}_{1,k} + jQ^{*}_{1,k}$.
3) A reference design stage creates the Fourier coefficients setpoints of the pulse pattern, $\boldsymbol{x}^{*}_{k}$. For $n > 1$, their phase is adjusted to match the harmonics of a distorted grid voltage with respect to the converter.
4) The proposed RT-OPP is a QP that optimizes a pulse pattern to embody the Fourier coefficient setpoints, $\boldsymbol{x}^{*}_{k}$. It sequentially adjusts the switching angles, $\Delta\boldsymbol{\alpha}_k$, from $\boldsymbol{\alpha}^{0}_{k}$ to yield the optimal switching angles, $\boldsymbol{\alpha}^{\text{opt}}_{k+1}$. To begin, $\boldsymbol{\alpha}^{0}_{k}$, can be initialized with a nominal pulse pattern from an LUT or ANN [23]. Then, $\boldsymbol{\alpha}^{0}_{k}$ is set to the previous solution, $\boldsymbol{\alpha}^{\text{opt}}_{k}$, to accumulate the consecutive adjustments in switching angles.

A. Steady-State Kalman Filter

To estimate the harmonic components of a distorted grid voltage, a Kalman filter (KF) can be used [31], [32], [33], [34]. Compared to Discrete Fast Fourier Transforms, a KF can accurately estimate a few harmonics of interest, rather than an entire spectrum. Moreover, it introduces less delay since it does not use large windows of time-domain data.

The design of a KF to estimate grid voltage harmonics begins with a quadrature-oscillator model for the nth harmonic

$$\underbrace{\begin{bmatrix} v_{\alpha;n,k+1} \\ v_{\beta;n,k+1} \end{bmatrix}}_{\boldsymbol{v}_{n,k+1}} = \underbrace{\begin{bmatrix} \cos(n\omega_1 t_s) & -\sin(n\omega_1 t_s) \\ \sin(n\omega_1 t_s) & \cos(n\omega_1 t_s) \end{bmatrix}}_{\boldsymbol{A}_n} \cdot \underbrace{\begin{bmatrix} v_{\alpha;n,k} \\ v_{\beta;n,k} \end{bmatrix}}_{\boldsymbol{v}_{n,k}} \tag{6}$$

where t_s is the sampling period and ω_1 is the fundamental frequency. For notational brevity, the $\alpha\beta$ subscript is omitted from the complete state vector for the nth harmonic. An advantage of $\boldsymbol{v}_{n,k}$ being in the $\alpha\beta$ frame is that its phase can be directly computed: $\theta_{n,k} = \tan^{-1}(v_{\beta;n,k}/v_{\alpha;n,k})$.

This simple quadrature model in (6) can then be extrapolated for up to N harmonics. In addition, as proposed in [22], a residual harmonics state, $\boldsymbol{v}_{\text{res},k}$, is appended to accumulate the unmodeled harmonics

$$\underbrace{\begin{bmatrix} \boldsymbol{v}_{1,k+1} \\ \vdots \\ \boldsymbol{v}_{N,k+1} \\ \boldsymbol{v}_{res,k+1} \end{bmatrix}}_{\boldsymbol{v}_{h,k+1}} = \underbrace{\begin{bmatrix} \boldsymbol{A}_1 & \cdots & \boldsymbol{0} & \boldsymbol{0} \\ \vdots & \ddots & \vdots & \vdots \\ \boldsymbol{0} & \cdots & \boldsymbol{A}_N & \boldsymbol{0} \\ \boldsymbol{0} & \cdots & \boldsymbol{0} & \boldsymbol{A}_{res} \end{bmatrix}}_{\boldsymbol{A}} \cdot \underbrace{\begin{bmatrix} \boldsymbol{v}_{1,k} \\ \vdots \\ \boldsymbol{v}_{N,k} \\ \boldsymbol{v}_{res,k} \end{bmatrix}}_{\boldsymbol{v}_{h,k}} . \tag{7}$$

Assuming a constant fundamental frequency, (7) is a linear time-invariant (LTI) system. Therefore, the recursive KF algorithm can be streamlined to an SSKF with a constant estimation gain [35]. Using the familiar Luenberger Observer, the state estimation law is

$$\hat{\boldsymbol{v}}_{h,k+1} = \boldsymbol{A} \cdot \hat{\boldsymbol{v}}_{h,k} + \boldsymbol{L}\left(\boldsymbol{v}_k - \hat{\boldsymbol{v}}_k\right) \tag{8}$$

where

$$\underbrace{\begin{bmatrix} \hat{v}_\alpha \\ \hat{v}_\beta \end{bmatrix}}_{\hat{\boldsymbol{v}}_k} = \underbrace{\begin{bmatrix} \boldsymbol{I} & \cdots & \boldsymbol{I} & \boldsymbol{I} \end{bmatrix}}_{\boldsymbol{C}} \hat{\boldsymbol{v}}_{h,k} \tag{9}$$

models the estimated grid voltage in the $\alpha\beta$ frame as the sum of all harmonic states. For the output measurement, a Clarke Transform is applied to the grid voltage, $\boldsymbol{v}_k = \boldsymbol{T}^{abc}_{\alpha\beta} \cdot \boldsymbol{v}_{g,k}$.

To determine the optimal estimation gain, $\boldsymbol{L}$, the duality between control and estimation can be applied to the Discrete-time Algebraic Ricatti Equation (DARE)

$$\boldsymbol{A}(\boldsymbol{P} - \boldsymbol{P}\boldsymbol{C}^T(\boldsymbol{R}_f + \boldsymbol{C}\boldsymbol{P}\boldsymbol{C}^T)^{-1}\boldsymbol{C}\boldsymbol{P})\boldsymbol{A}^T + \boldsymbol{Q}_f = \boldsymbol{P} \tag{10}$$

where $\boldsymbol{Q}_f$ and $\boldsymbol{R}_f$ are the respective process and measurement covariance matrices that couple white Gaussian noise into (7). Solving (10) for $\boldsymbol{P}$ yields the optimal estimation gain

$$\boldsymbol{L} = \boldsymbol{A}\boldsymbol{P}\boldsymbol{C}^T(\boldsymbol{R} + \boldsymbol{C}\boldsymbol{P}\boldsymbol{C}^T)^{-1}. \tag{11}$$

To design an SSKF, the output sensor's covariance can be measured to give $\boldsymbol{R}_f$. Whereas for $\boldsymbol{Q}_f$, this encapsulates any parameter or modeling uncertainties, so designing it is an iterative process [36]. To ensure the residual harmonics state is a multifrequency bin that accumulates unmodeled harmonics, a higher process covariance is assigned to it

$$\boldsymbol{Q}_f = \rho_{\text{obs}} \cdot \text{diag}\left[\boldsymbol{I} \cdots \boldsymbol{I}, 10 \cdot \boldsymbol{I}\right]. \tag{12}$$

The scalar parameter ρ_{obs} can be adjusted to fine-tune the desired bandwidth and estimation performance.

To demonstrate how the residual harmonics state can improve estimation performance without needing to model many harmonics, numerical results of two SSKFs are compared in Fig. 4. The sample rates are set to 5 kHz and $\rho_{\text{obs}} = \max(\boldsymbol{R}_f)$. Remarks for each sub-figure will now be given

In Fig. 4(a), the standard SSKF's estimated fundamental, $\hat{v}_{\alpha;1}$, and 5th voltage harmonic, $\hat{v}_{\alpha;5}$, are corrupted upon distorting the grid voltage. Recalling (9), this occurs since $\hat{v}_\alpha$ must be completely reconstructed by summing $\hat{v}_{\alpha;1}$ and $\hat{v}_{\alpha;5}$. Consequently, the unmodeled 7th, 11th, and 13th harmonics are forced into these states.

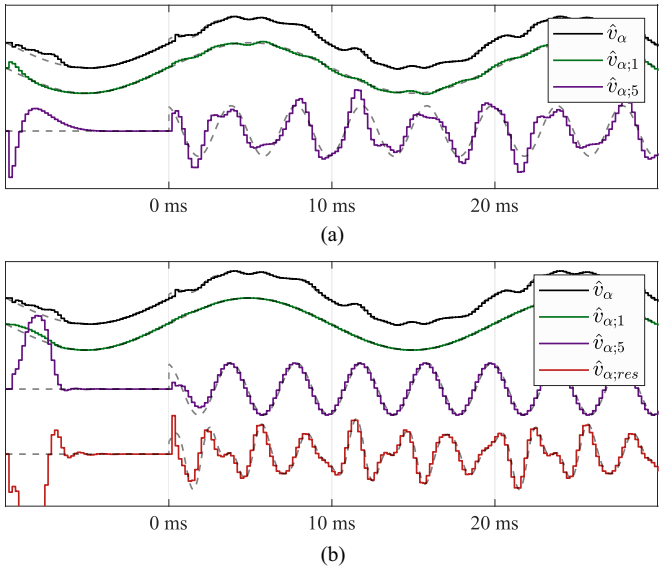

Fig. 4. Numerical results comparing two SSKFs that estimate the fundamental and 5th harmonic of a distorted grid voltage. At t =0ms, a step distortion of the 5th–13th NTO harmonics is applied. The dotted grey lines indicate the true state which the SSKF is tasked with estimating. (a) Standard SSKF with no residual harmonic state. (b) Improved SSKF with residual harmonic state, shown in red, to accumulate the unmodelled harmonics.

In Fig. 4(b), a residual harmonics state is included to improve the SSKF's estimation performance. Examining $\hat{v}_{\alpha;\text{res}}$, it accumulates the unmodeled 7th, 11th, and 13th harmonics to prevent $\hat{v}_{\alpha;1}$, and $\hat{v}_{\alpha;5}$ from being incorrectly estimated. Furthermore, the residual harmonics state ensures the estimation performance of an SSKF for a distorted grid voltage is independent from the number of modeled harmonics.

For the remainder of this proposal, the residual harmonic state, $\boldsymbol{v}_{\text{res},k}$, is not required by the downstream stages. It is just an internal state to improve the SSKF's performance. Moving forward, it is discarded and the estimated states are truncated to $\mathcal{N}_{\text{mod}}$ grid voltage harmonics

$$\hat{\boldsymbol{v}}_{h,k} = [\hat{\boldsymbol{v}}_{1,k} \cdots \hat{\boldsymbol{v}}_{n,k} \cdots \hat{\boldsymbol{v}}_{N,k}]^T. \tag{13}$$

Note that $\hat{\boldsymbol{v}}_{1,k}$ is used in the succeeding Section III-B for the power controller stage and then later replaced by $\boldsymbol{v}^*_{i,k}$ in Section III-C for the reference design stage.

B. Power Controller

To control the power flow in a grid-connected converter, a standard voltage-oriented control (VOC) strategy in the synchronous dq frame will be used. A block diagram of this popular control strategy is shown in Fig. 9.18 and thoroughly described in Ref. [2, Sec. 9.4.1].

To suit the proposal, two changes to the typical VOC structure have been made

1) The grid voltage component is the estimated fundamental, $\hat{\boldsymbol{v}}_{1,k}$, from the upstream SSKF – not the complete measurement, $\boldsymbol{v}_{g,k}$. This removes the need to filter out the harmonics of a distorted grid voltage from the feedforward component and calculation of $\vec{S}^*_{1,k}$. In addition, this also removes the need for a PLL. The phase of the grid voltage is conveniently yielded from the SSKF's estimate of the fundamental grid voltage component, $\hat{\theta}_{g;1} = \tan^{-1}(\hat{v}_{\beta;1}/\hat{v}_{\alpha;1})$.
2) The input voltage setpoint is kept in the stationary $\alpha\beta$ frame, $\boldsymbol{v}^*_{1,k} = [v^*_{\alpha;1}, v^*_{\beta;1}]^T$, for the reference design stage. This allows the estimated grid voltage harmonic's phase to be adjusted with respect to the converter.

C. Reference Design

Given an input voltage setpoint, $\boldsymbol{v}^*_{1,k}$, and the estimated grid voltage harmonics, $\hat{\boldsymbol{v}}_{h,k}$, the reference design stage yields the Fourier coefficient setpoints, $\boldsymbol{x}^*_k$, for RT-OPP. This stage can be consolidated into a set of transformations

$$\boldsymbol{x}^*_k = \boldsymbol{T}^* \cdot \boldsymbol{v}^*_k \tag{14}$$

where

$$\begin{aligned} \boldsymbol{x}^*_k &= [\boldsymbol{x}^*_{1,k} \cdots \boldsymbol{x}^*_{n,k} \cdots \boldsymbol{x}^*_{N,k}]^T \\ \boldsymbol{T}^* &= [\boldsymbol{T}^*_1 \cdots \boldsymbol{T}^*_n \cdots \boldsymbol{T}^*_N] \\ \boldsymbol{v}^*_k &= [\boldsymbol{v}^*_{1,k} \cdots \boldsymbol{v}^*_{n,k} \cdots \boldsymbol{v}^*_{N,k}]^T. \end{aligned} \tag{15}$$

Note that for $1 < n \leq N$, the voltage setpoints are the estimated grid voltage harmonics from the SSKF, $\boldsymbol{v}^*_{n,k} = \hat{\boldsymbol{v}}_{n,k}$. The remainder of this section is focused on explaining the setpoint transformation, $\boldsymbol{T}^*_n$.

Since $\boldsymbol{v}^*_{1,k}$ and $\hat{\boldsymbol{v}}_{h,k}$ are in the $\alpha\beta$ frame, a Park Transform, $\boldsymbol{T}^{\alpha\beta}_{dq}$, can extract the nth harmonic's dq components, such that $\vec{v}_n = d_n + jq_n$. Recalling (1), the Fourier coefficients in Cartesian coordinates are similarly $\vec{x_n} = a_n - jb_n$. Therefore, by inverting the quadrature axis, it is aligned with b_n. However, for negative-sequence harmonics, their reversed rotation negates this inversion, so $b_n = -\text{sign}(n) \cdot q_n$.

To yield the nth Fourier coefficient setpoint, $\boldsymbol{x}^*_{n,k}$, the respective setpoint transformation, $\boldsymbol{T}^*_n$, is given by

$$\underbrace{\begin{bmatrix} a^*_n \\ b^*_n \end{bmatrix}}_{\boldsymbol{x}^*_{n,k}} = \underbrace{\begin{bmatrix} 1 & 0 \\ 0 & -\text{sign}(n) \end{bmatrix} \cdot \boldsymbol{T}^{\alpha\beta}_{dq}}_{\boldsymbol{T}^*_n} \cdot \underbrace{\begin{bmatrix} v^*_{\alpha;n} \\ v^*_{\beta;n} \end{bmatrix}}_{\boldsymbol{v}^*_{n,k}}. \tag{16}$$

The Park Transform, $\boldsymbol{T}^{\alpha\beta}_{dq}$, is synchronized with the fundamental input voltage setpoint, $\theta^*_1 = \tan^{-1}(v^*_{\beta;1}/v^*_{\alpha;1})$, instead of the grid voltage, $\hat{\theta}_{g;1}$. Otherwise, the phase of each voltage harmonic applied by the converter would not track the respective grid voltage harmonic as θ^*_1 is displaced from $\hat{\theta}_{g;1}$ when power is flowing. To account for this phase shift introduced by a grid-connected converter, the Park Transform in (16) is given by

$$\boldsymbol{T}^{\alpha\beta}_{dq} = \begin{bmatrix} \cos(n\theta^*_1) & \sin(n\theta^*_1) \\ -\sin(n\theta^*_1) & \cos(n\theta^*_1) \end{bmatrix}. \tag{17}$$

For the Reference Design stage, the $n > 1$ Fourier coefficient setpoints, $\boldsymbol{x}^*_{n,k}$, are the magnitude and phase of each estimated grid voltage harmonic with respect to the converter. Therefore,

tracking these setpoints will compensate for a distorted grid voltage.

D. Quadratic Program

Optimizing a pulse pattern to perfectly embody all Fourier coefficient setpoints, $\boldsymbol{x}_k = \boldsymbol{x}_k^*$, may not always be possible. Therefore, the objective is to control the converter's fundamental component while mitigating the effect of grid voltage harmonics. To do so, this work proposes to streamline the incumbent NLP optimization problem from (4) into a QP for efficient solving in real-time.

A pragmatic approach to ease the computational burden of optimizing pulse patterns is to simplify their nonlinear Fourier coefficients (2). To do so, the ith switching angle from the set $\boldsymbol{\alpha}$ can be split into $\alpha_i = \alpha_i^0 + \Delta\alpha_i$. There are now two switching angles – the nominal, α_i^0, and an adjustment term, $\Delta\alpha_i$. Then, the trigonometric expressions in (2) can be separated by applying the angle sum and difference identity

$$\cos(\alpha_i^0 \pm \Delta\alpha_i) = \cos(\alpha_i^0)\cdot\cos(\Delta\alpha_i) \mp \sin(\alpha_i^0)\cdot\sin(\Delta\alpha_i) \tag{18a}$$

$$\sin(\alpha_i^0 \pm \Delta\alpha_i) = \sin(\alpha_i^0)\cdot\cos(\Delta\alpha_i) \pm \cos(\alpha_i^0)\cdot\sin(\Delta\alpha_i). \tag{18b}$$

For α_i^0, it can be initialized from a LUT, or as later suggested, the previous set of switching angles.

If $\Delta\alpha_i$ is small, then $\cos(\Delta\alpha_i) \approx 1$ and $\sin(\Delta\alpha_i) \approx \Delta\alpha_i$. Substituting these approximations into (18) yields a linear expression with respect to $\Delta\alpha_i$ when α_i^0 is held constant

$$\cos(\alpha_i^0 \pm \Delta\alpha_i) \approx \cos(\alpha_i^0) \mp \Delta\alpha_i\cdot\sin(\alpha_i^0) \tag{19a}$$

$$\sin(\alpha_i^0 \pm \Delta\alpha_i) \approx \sin(\alpha_i^0) \pm \Delta\alpha_i\cdot\cos(\alpha_i^0). \tag{19b}$$

A dynamic interpretation of (19) is a difference equation, where $\Delta\alpha_{i,k}$ is a small linear update from $\alpha_{i,k}^0$ to yield $\alpha_{i,k+1}^0$

$$\cos(\alpha_{i,k+1}^0) \approx \cos(\alpha_{i,k}^0) - \Delta\alpha_{i,k}\cdot\sin(\alpha_{i,k}^0) \tag{20a}$$

$$\sin(\alpha_{i,k+1}^0) \approx \sin(\alpha_{i,k}^0) + \Delta\alpha_{i,k}\cdot\cos(\alpha_{i,k}^0). \tag{20b}$$

Applying (20) to (2), the dynamic bilinear expression for the nth harmonic's HWS Fourier Coefficients is given by

$$a_n(\boldsymbol{\alpha}_{k+1}^0) \approx \frac{-2}{n\pi}\sum_{i=1}^{2d}\Delta u_i\left[\sin(n\alpha_{i,k}^0) + n\Delta\alpha_{i,k}\cos(n\alpha_{i,k}^0)\right] \tag{21a}$$

$$b_n(\boldsymbol{\alpha}_{k+1}^0) \approx \frac{2}{n\pi}\sum_{i=1}^{2d}\Delta u_i\left[\cos(n\alpha_{i,k}^0) - n\Delta\alpha_{i,k}\sin(n\alpha_{i,k}^0)\right] \tag{21b}$$

where

$$\boldsymbol{\alpha}_k^0 = \left[\alpha_{1,k}^0 \cdots \alpha_{2d,k}^0\right], \quad \Delta\boldsymbol{\alpha}_k = \left[\Delta\alpha_{1,k} \cdots \Delta\alpha_{2d,k}\right]. \tag{22}$$

Examining (21), it is a dynamic linear model with respect to $\Delta\boldsymbol{\alpha}_k$ when $\boldsymbol{\alpha}_k^0$ is held constant. Whereas (2) is static and nonlinear with respect to $\boldsymbol{\alpha}$. Despite their differences, (21) correctly converges to (2) as $\Delta\boldsymbol{\alpha}_k \to 0$.

The constant and coefficient terms in (21) can be separated to yield a more compact expression

$$\underbrace{\begin{bmatrix} a_n \\ b_n \end{bmatrix}}_{\boldsymbol{x}_{n,k+1}} = \underbrace{\begin{bmatrix} a_n \\ b_n \end{bmatrix}}_{\boldsymbol{x}_{n,k}} - n\underbrace{\begin{bmatrix} b_{n,1} & \cdots & b_{n,2d} \\ a_{n,1} & \cdots & a_{n,2d} \end{bmatrix}}_{\boldsymbol{B}_{n,k}(\boldsymbol{x}_k)}\underbrace{\begin{bmatrix} \Delta\alpha_1 \\ \vdots \\ \Delta\alpha_{2d} \end{bmatrix}}_{\Delta\boldsymbol{\alpha}_k}. \tag{23}$$

The k and $k+1$ subscripts are omitted from the expanded matrices for notational brevity.

The Fourier coefficients, $\boldsymbol{x}_{n,k}$, are evaluated at $\boldsymbol{\alpha}_k^0$ using (2). As are $a_{n,i}$ and $b_{n,i}$, where each column in $\boldsymbol{B}_{n,k}(\boldsymbol{x}_k)$ is the ith switching angle from the summation in (2).

Furthermore, (23) can be extrapolated up to Nth harmonic to yield a dynamic bilinear model of a pulse pattern's HWS Fourier coefficients

$$\underbrace{\begin{bmatrix} \boldsymbol{x}_1 \\ \vdots \\ \boldsymbol{x}_N \end{bmatrix}}_{\boldsymbol{x}_{k+1}} = \underbrace{\begin{bmatrix} \boldsymbol{x}_1 \\ \vdots \\ \boldsymbol{x}_N \end{bmatrix}}_{\boldsymbol{x}_k} - \underbrace{\begin{bmatrix} \boldsymbol{B}_1(\boldsymbol{x}_1) \\ \vdots \\ \boldsymbol{B}_N(\boldsymbol{x}_N) \end{bmatrix}}_{\boldsymbol{B}_k(\boldsymbol{x}_k)}\underbrace{\begin{bmatrix} \Delta\alpha_1 \\ \vdots \\ \Delta\alpha_{2d} \end{bmatrix}}_{\Delta\boldsymbol{\alpha}_k}. \tag{24}$$

The k and $k+1$ subscripts are omitted from the expanded matrices for notational brevity.

Based on this dynamic bilinear model (24) of the voltage harmonics in a pulse pattern, the NLP from (4) can be approximated into the following QP:

$$\min_{\Delta\boldsymbol{\alpha}_k} \quad f(\Delta\boldsymbol{\alpha}_k) = \underbrace{\boldsymbol{x}_e^T\cdot\boldsymbol{Q}\cdot\boldsymbol{x}_e}_{\text{WTHD}} + \lambda_u\cdot\underbrace{\Delta\boldsymbol{\alpha}_k^T\cdot\Delta\boldsymbol{\alpha}_k}_{||\Delta\boldsymbol{\alpha}_k||^2}.$$

Subject to :

$$0 \le \alpha_i^0 + \Delta\alpha_i \le \cdots \le \alpha_{2d}^0 + \Delta\alpha_{2d} \le \pi \tag{25}$$

where

$$\boldsymbol{x}_e = \boldsymbol{x}_{k+1}^* - \boldsymbol{x}_{k+1} \qquad \boldsymbol{Q} = \operatorname{diag}(q_1 \cdots q_N). \tag{26}$$

Examining the two quadratic terms in (25), first, the weighted THD (WTHD) is set by the positive-definite diagonal matrix $\boldsymbol{Q}$. The nth diagonal element of $\boldsymbol{Q}$ is q_n from (4). This biases the error in Fourier coefficients, $\boldsymbol{x}_e$, to tailor the pulse pattern's spectrum toward a harmonic objective.

Second, the squared magnitude of switching angle adjustments, $||\Delta\boldsymbol{\alpha}_k||^2$, is biased by the scalar penalty, λ_u. This assists in limiting $\Delta\boldsymbol{\alpha}_k$ to safeguard the small angle approximation's accuracy, as will be shown in Section III-E.

Assuming $\Delta\boldsymbol{\alpha}_k$ is kept small, the ascending inequality constraint can be enforced retrospectively. From this, (25) can be cast as an unconstrained QP. Therefore, at the kth instant, (25) is minimized by solving

$$\frac{\partial f(\Delta\boldsymbol{\alpha}_k)}{\partial\Delta\boldsymbol{\alpha}_k} = 0. \tag{27}$$

Using the common derivative identities of a quadratic, $\frac{\partial}{\partial x}(\boldsymbol{x}^T\boldsymbol{Q}\boldsymbol{x}) = 2\boldsymbol{Q}\boldsymbol{x}$, and linear term, $\frac{\partial}{\partial x}(\boldsymbol{x}^T\boldsymbol{Q}) = \boldsymbol{Q}^T$, the optimal analytic update policy to minimize (25) is

$$\Delta\boldsymbol{\alpha}_k^{opt} = \boldsymbol{K}_k\cdot(\boldsymbol{x}_k^* - \boldsymbol{x}_k) \tag{28}$$

Algorithm 1: RT-OPP.

Given $\boldsymbol{x}_k^*$

1) Form $\boldsymbol{x}_k$ and $\boldsymbol{B}_k$ of the bilinear dynamic model for the $\mathcal{N}_{mod}$ harmonics linearised at $\boldsymbol{\alpha}_k^0$.
2) Evaluate the optimal analytic update policy, $\Delta\boldsymbol{\alpha}_k^{opt} = \boldsymbol{K}_k \cdot (\boldsymbol{x}_k^* - \boldsymbol{x}_k)$
3) Adjust the switching angles from their initial point, $\boldsymbol{\alpha}_{k+1}^{opt} = \Delta\boldsymbol{\alpha}_k^{opt} + \boldsymbol{\alpha}_k^0$
4) Enforce the ascending inequality constraint, $0 \leq \alpha_1^{opt} \leq \cdots \leq \alpha_{2\,d}^{opt} \leq \pi$

Return $\boldsymbol{\alpha}_k^{opt}$ and update initial point, $\boldsymbol{\alpha}_{k+1}^0 \leftarrow \boldsymbol{\alpha}_{k+1}^{opt}$.

where

$$\begin{aligned} \boldsymbol{K}_k &= \boldsymbol{W}_k^{-1} \cdot \boldsymbol{F}_k \\ \boldsymbol{W}_k &= \boldsymbol{B}_k^T \cdot \boldsymbol{Q} \cdot \boldsymbol{B}_k + \lambda_u \cdot \boldsymbol{I} \\ \boldsymbol{F}_k &= \boldsymbol{B}_k^T \cdot \boldsymbol{Q}. \end{aligned} \tag{29}$$

For notational brevity, $\boldsymbol{B}_k = \boldsymbol{B}_k(\boldsymbol{x}_k)$.

The optimal adjustment gain, $\boldsymbol{K}_k$, is computed by solving a linear system of equations – this requires a fixed number of arithmetic operations. Therefore, (25) can be minimized at a precise rate using the optimal analytic update policy (28).

Upon evaluating (28), the initial switching angles are then shifted from $\boldsymbol{\alpha}_k^0$ by $\Delta\boldsymbol{\alpha}_k^{\text{opt}}$, to yield

$$\boldsymbol{\alpha}_{k+1}^{\text{opt}} = \Delta\boldsymbol{\alpha}_k^{\text{opt}} + \boldsymbol{\alpha}_k^0. \tag{30}$$

Since $\Delta\boldsymbol{\alpha}_k$ must be kept small, it is proposed to minimize (25) in a sequential manner

$$\boldsymbol{\alpha}_{k+1}^0 = \boldsymbol{\alpha}_{k+1}^{\text{opt}}. \tag{31}$$

Such an approach is inspired from the Newton's Method step of an SQP. By setting the next initial point as the present solution, sequentially small steps in $\Delta\boldsymbol{\alpha}_k$ accumulate to yield larger changes to the Fourier coefficients. Recalling the ascending inequality constraints in (25), they are enforced on $\boldsymbol{\alpha}_k^{\text{opt}}$ prior to assigning $\boldsymbol{\alpha}_{k+1}^0$ – in between (30) and (31).

In all, the proposed RT-OPP can be distilled into an optimization algorithm, as given by the listing in Algorithm 1.

Note that $\boldsymbol{\alpha}_k^0$ is initialized from a nominal pulse pattern, such as the LUTs shown in Fig. 2. If m^* were to change, then $\boldsymbol{\alpha}_k^0$ could be reinitialized to restart RT-OPP from this new nominal pulse pattern.

E. Design Guidelines for Switching Angle Adjustment Penalty

To provide guidelines for designing λ_u, its effect on $\Delta\boldsymbol{\alpha}_k^{\text{opt}}$ for three different values, $\lambda_u \in \{0.1, 0.05, 0.01\}$, will be explored using numerical results.

Upon distorting the grid voltage with the 5th–13th NTO harmonics, RT-OPP is challenged with uniformly rejecting, $\boldsymbol{Q} = \boldsymbol{I}$, them with $d = 5$ switching angles. $\boldsymbol{\alpha}_k^0$ is initialized from the SHE LUT in Fig. 2(a) at $m^* = 1.1377$ and the sample rate for RT-OPP is set to $f_s = 5$ kHz.

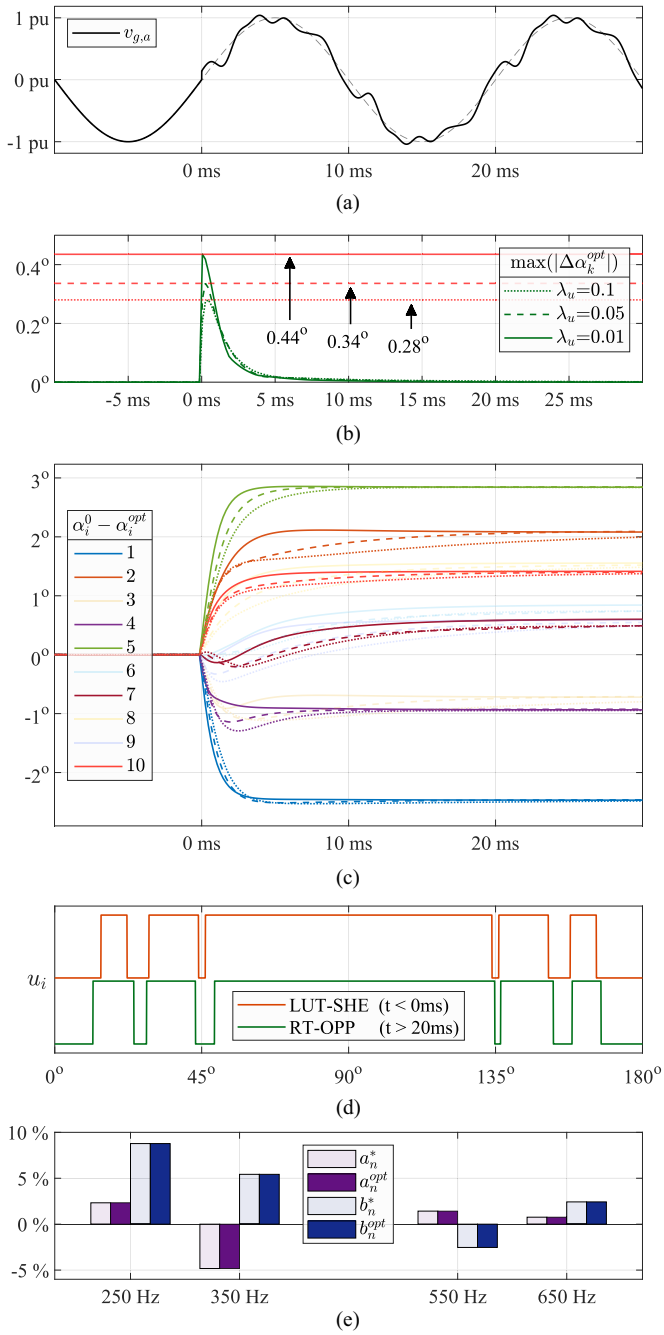

Fig. 5. Numerical results of RT-OPP illustrating the effect of λ_u on $\Delta\boldsymbol{\alpha}_k$ for $\lambda_u \in \{0.1, 0.05, 0.01\}$. (a) Grid voltage. (b) Maximum switching angle adjustments. (c) Adjustments from SHE LUT. (d) Half-cycle comparison of SHE and RT-OPP. (e) Steady-state setpoint tracking of Fourier coefficients.

The numerical results are presented in Fig. 5 and remarks for each sub-figure will now be given.

In Fig. 5(a), the grid voltage is stepped from ideal to distorted at $t = 0$ ms. The pu magnitude and phase of the 5th–13th NTO grid voltage harmonics are set to

$$\begin{aligned} \vec{v}_{g,5} &= 0.10\angle 105^\circ & \vec{v}_{g,11} &= 0.04\angle 350^\circ \\ \vec{v}_{g,7} &= 0.08\angle 85^\circ & \vec{v}_{g,13} &= 0.02\angle 255^\circ. \end{aligned} \tag{32}$$

In Fig. 5(b), upon distorting the grid voltage, a tracking error in Fourier coefficients is introduced and the RT-OPP algorithm begins adjusting the switching angles. The maximum adjustments for all three cases are shown with annotations added for their respective peaks. As λ_u is decreased from 0.1 to 0.01, the peak $\Delta\boldsymbol{\alpha}_k^{\text{opt}}$ increases from 0.28° to 0.44°. This implies an inverse relationship between λ_u and $||\Delta\boldsymbol{\alpha}_k^{\text{opt}}||^2$.

In Fig. 5(c), the optimized switching angles, $\boldsymbol{\alpha}_k^{\text{opt}}$, adjusted from the SHE LUT are shown. Of the ten switching angles RT-OPP is adjusting, a select few are highlighted. As seen by comparing the solid, dashed and dotted lines, λ_u adjusts the trajectory of switching adjustments. Yet for all cases, $\boldsymbol{\alpha}_k^{\text{opt}}$ converges on the same values since $\boldsymbol{Q}$ is kept constant. This verifies λ_u is decoupled from the harmonic objective.

In Fig. 5(d), the positive half-cycles of the initialized LUT SHE pulse pattern to that yielded by RT-OPP after 20 ms are compared. By sequentially updating the initial switching angles between optimizations, $\boldsymbol{\alpha}_{k+1}^0 \leftarrow \boldsymbol{\alpha}_{k+1}^{\text{opt}}$, small and accurate adjustments accumulate to noticeable changes.

In Fig. 5(e), to verify that RT-OPP has compensated for the distorted grid voltage, the Fourier coefficients are compared against their setpoints. As intended, RT-OPP has successfully minimized $\boldsymbol{x}_e$ to match the magnitude and phase of the 5th–13th NTO grid voltage harmonics.

The key observation from these numerical results is that λ_u is inversely proportional to $||\Delta\boldsymbol{\alpha}_k^{\text{opt}}||^2$

$$\lambda_u \propto \frac{1}{||\Delta\boldsymbol{\alpha}_k^{\text{opt}}||^2}. \tag{33}$$

Therefore, λ_u is an effective means to safeguard the small angle approximation used in formulating the dynamic bilinear model (24)—provided it is not set too small. As suggested by (33), the appropriate value for λ_u is dependent on the desired magnitude of switching angle adjustments. For an initial design, it is recommended to first set $\lambda_u = 0.01$ and then tune further if needed.

Most importantly, it has been shown that λ_u affects the trajectory of $\boldsymbol{\alpha}_k^{\text{opt}}$, not its final value. This maintains an emphasis on $\boldsymbol{Q}$ to tailor the harmonic objective.

IV. Experimental Results

Having proposed a quadratic optimization algorithm to compute pulse patterns that compensate for distorted grid voltages, the focus is now executing it in real-time. To acquire experimental results, RT-OPP is implemented in C++ on a standard microcontroller.

The proposed RT-OPP and all supporting stages shown in Fig. 3 are executed at $f_s = 5$ kHz on an STM32H7RS microcontroller. For the grid-connected 3L-NPC converter system, a hardware-in-loop (HIL) setup is adopted by modeling a digital twin on an OPAL-RT 4510 using the parameters given in Appendix A. The grid voltage and current are the analog outputs, whereas the gate drive signals are the digital inputs. An image of the laboratory setup is given in Appendix B.

For the experimental results, two contrasting harmonic objectives are explored to demonstrate the proposal's versatility—SHC in Section IV-A and HDM in Section IV-B. The initial points for SHC and HDM are, respectively, extracted from the nominal SHE and OPP LUTs in Fig. 2. From then on, the initial point is sequentially updated, $\boldsymbol{\alpha}_{k+1}^0 \leftarrow \boldsymbol{\alpha}_{k+1}^{\text{opt}}$. For both cases, the grid voltage is stepped from ideal to distorted (32). Throughout this transient, the power controller's setpoint is kept constant at maximum active power $\vec{S}_{1,k}^* = 1\angle 0°$ p · u.

TABLE I
RT-OPP Design for SHC

Parameter	Symbol	Values
Selected NTO Harmonics	$\mathcal{N}_{mod}$	5 (up to 13th)
Tracking Error Penalty	$\boldsymbol{Q}$	diag([1, 1, 1, 1, 1])
Adjustment Penalty	λ_u	0.01

Monte-carlo results for HDM are additionally presented to explore the proposal's effectiveness for 10 000 randomly distorted grid voltages. Then, execution times of RT-OPP performing SHC and HDM are discussed and compared against incumbent NLP approaches in Section IV-C.

A. Selective Harmonic Control

For SHC, the objective is to control the 5th–13th NTO harmonics to match their respective grid voltage harmonics. In doing so, the corresponding grid current harmonics are then eliminated—much like SHE. To indiscriminately control a selected number of harmonics, $\boldsymbol{Q}$ is set to an identity matrix. The design of RT-OPP for SHC is given in Table I.

The experimental results of RT-OPP for SHC are shown in Fig. 6 and remarks for each sub-figure will now be given

In Fig. 6(a), RT-OPP has adjusted a pulse pattern to reject the 5th–13th NTO grid voltage harmonics within less than 10 ms from distorting the grid voltage. During this transient, RT-OPP demonstrates excellent tracking performance and each harmonic correctly settles to their setpoints, as shown by the dashed-dotted lines.

In Fig. 6(b), the SHE pulse pattern from an LUT, shown in orange, is initialized as $\boldsymbol{\alpha}_k^0$ for RT-OPP. The green pulse pattern is yielded by RT-OPP after 10 ms; as seen by examining $v_{i,abc}$ in Fig. 6(a). The converter's grid current waveforms when subjected to this distorted grid voltage are then shown below the respective pulse patterns. Examining the magnitude spectrum of these currents, $|i_{g,a}|$, the susceptibility of an SHE LUT pulse pattern to grid voltage harmonics is evidenced by large magnitudes of the 5th–13th NTO harmonics. Whereas for RT-OPP, by simply adjusting this precomputed SHE pattern, it has eliminated these current harmonics. This verifies that the proposed RT-OPP has successfully compensated for this distorted grid voltage.

B. Harmonic Distortion Minimization

For HDM, the objective is to minimize a broader spectrum of harmonics. To do so, RT-OPP is extended up to the 49th harmonic by setting $\mathcal{N}_{\text{mod}} = 17$. To reduce THDi for an RL output filter, the voltage harmonics are penalized with the diagonal entries of $\boldsymbol{Q}$ set to $q_n = 1/n^2$ – like an OPP.

The same Reference Design from SHC is used – the Fourier coefficient setpoints match the estimated grid voltage harmonics with respect to the converter. In all, RT-OPP is tasked with

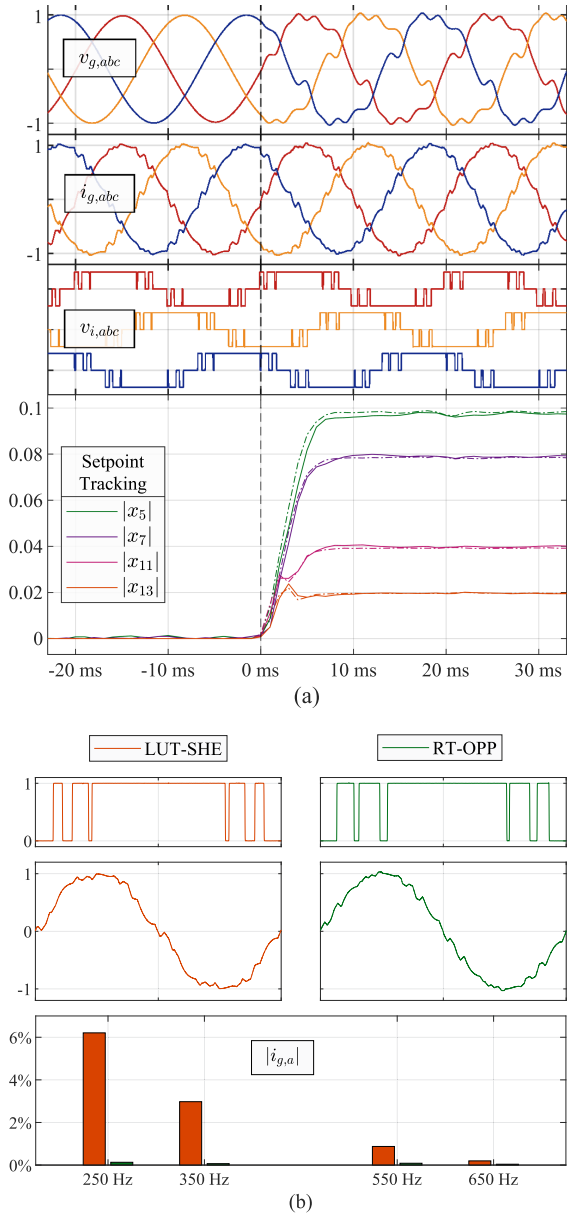

Fig. 6. Experimental results of the proposed RT-OPP performing SHC. (a) At t =0ms, the grid voltage, $v_{g,abc}$, is distorted with the 5th–13th NTO harmonics from (32). RT-OPP then adjusts the converter's SHE pulse pattern from an LUT to match the grid voltage harmonics, as shown by examining $v_{i,abc}$. The bottom plot depicts the setpoint tracking performance for the selected harmonics; the setpoints, $|\boldsymbol{x}_n^*|$, are shown by the dashed-dotted lines. (b) A half-cycle of the pulse patterns from an SHE LUT and RT-OPP are compared. Below this, the resultant grid current waveform from applying the above pulse patterns with the distorted grid voltage from (a) are, respectively, given. Then, the magnitude spectrum of these currents is shown for the 5th–13th NTO harmonics.

rejecting the 5th–13th grid voltage harmonics whilst eliminating the 17th–49th NTO harmonics with only $d = 5$ switching angles. This impossible objective is no different to compensating an OPP for grid voltage harmonics, as undertaken in [22]. The design of RT-OPP for HDM is summarised in Table II.

The experimental results of RT-OPP for HDM are shown in Fig. 7 and remarks for each sub-figure will now be given.

In Fig. 7(a), upon distorting the grid voltage at $t = 0$ ms, the converter's ripple current immediately increases. This is evident by examining the direct and quadrature grid current components

TABLE II
RT-OPP DESIGN FOR HDM

Parameter	Symbol	Values
Selected NTO Harmonics	$\mathcal{N}_{mod}$	17 (up to 49$^{\text{th}}$)
Tracking Error Penalty	$\boldsymbol{Q}$	diag($[1, 1/5^2, ..., 1/49^2]$)
Adjustment Penalty	λ_u	0.01

of the fundamental, $i_{d,1}$ and $i_{q,1}$. Within less than 10 ms after this transient, RT-OPP has adjusted the OPP from an LUT, $v_{i,abc}$, to reduce the current ripple.

In Fig. 7(b), the adjustments made by RT-OPP can be seen by comparing the orange and green pulse patterns. The orange is a nominal OPP from an LUT. RT-OPP is initialized from this and adjusts the switching angles to yield the green pulse pattern. Below are the grid current waveforms when the above pulse patterns are subjected to the distorted grid voltage – the reduction in current distortions from RT-OPP are visibly clear. To quantify this improvement, the magnitude spectrum and THDi are compared. By designing $\boldsymbol{Q}$ to minimize current harmonics, RT-OPP has adjusted an OPP to reduce THDi from 7.29% to 2.88%; an improvement of more than 50%.

To further analyze the proposed RT-OPP, a Monte-Carlo experiment is performed by repeating the above case 10 000 times for random grid voltage distortions. The goal is to understand how quickly RT-OPP can compensate for a distorted grid voltage to reduce THDi in real-time. This is key to verifying the potential of RT-OPP in practice, as the phase and magnitude of grid voltage harmonics are random and generally unknown.

The THDi is given with respect to the OPP from an LUT. The solving time from stepping an ideal grid voltage to a random distortion of the 5th–13th NTO harmonics is then recorded. The maximum magnitude is limited to 0.1 p · u· and the phase is unconstrained.

The Monte-Carlo results of RT-OPP for HDM are shown in Fig. 8 and remarks for each sub-figure will now be given.

In Fig. 8(a), on average, RT-OPP has reduced THDi from 6.32% to 5.05% within less than 100 ms; an improvement in harmonic performance of more than 25%. It is promising to highlight that 90% of this prospective improvement is delivered in almost a single 50 Hz cycle.

In Fig. 8(b), a histogram of the Monte-Carlo results is presented. Here, the red solid line indicates the mean reduction in THDi is 25%. One standard deviation of $\sigma = 11\%$ is shown by the red dotted lines. This implies that RT-OPP reduces THDi by 14% to 36% in more than 50% of cases.

Since RT-OPP performs local optimization from $\boldsymbol{\alpha}_k^0$, minimizing (25) may yield a sub-optimal solution. Whereas in [22], global optimization was performed using an NLP solver that iterates through a queue of quasi-random initial points. Compared to the Monte-Carlo results of this proposal, it yielded a larger reduction in THDi of 65% in 900 ms.

Despite a disparity in optimality, RT-OPP can complement cumbersome NLP solvers. For example, if a more optimal solution is found for a similar $\boldsymbol{x}_1^*$, RT-OPP can be restarted from it by simply updating $\boldsymbol{\alpha}_k^0$. From this new initial point, RT-OPP

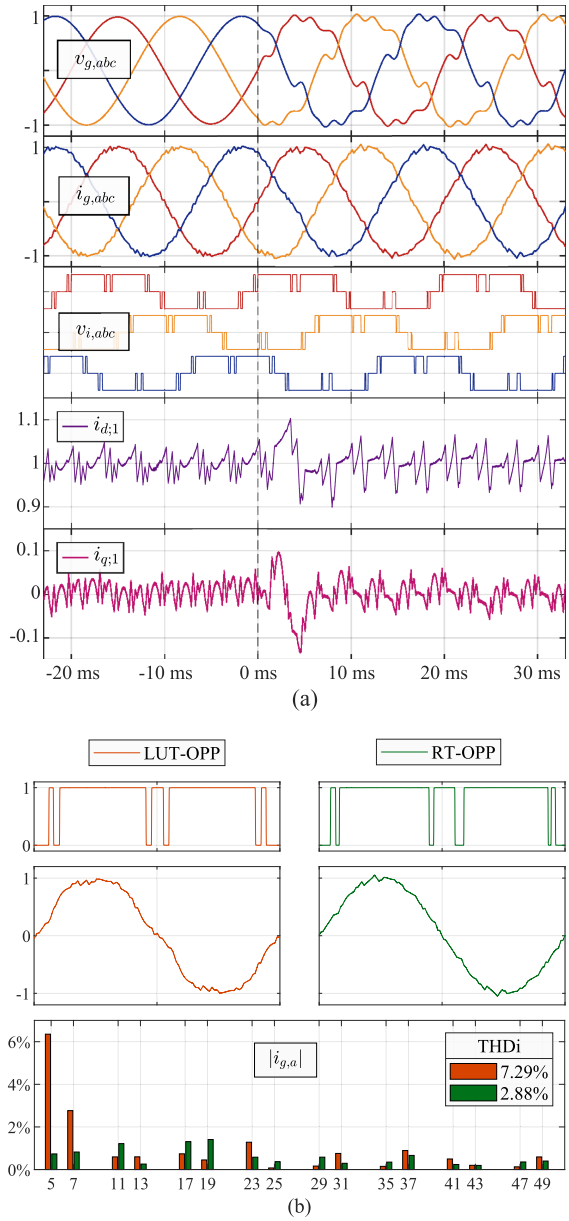

Fig. 7. Experimental results of the proposed RT-OPP performing HDM. (a) At t =0ms, the grid voltage, $v_{g,abc}$, is distorted with the 5th–13th NTO harmonics from (32). Examining the converter's voltage, $v_{i,abc}$, RT-OPP adjusts the OPP from a LUT to minimize the ripple current. This transient is shown by the dq components of the fundamental grid current, $i_{d;1}$ and $i_{q;1}$. (b) A half-cycle of an OPP from a LUT and the resulting by RT-OPP are shown. Below this, the grid current waveforms when subjected to the distorted grid voltage from (a) are respectively given. Then, the magnitude spectrum and THDi of these currents for NTO harmonics up to the 49th is shown.

can then refine the harmonic performance in real-time as small changes in grid voltage harmonics occur.

A final remark on RT-OPP for HDM, is the potential to enforce conformance to harmonic current limits, such as IEEE-519 [30]. Recalling that $\boldsymbol{x}_n^*$ and $\boldsymbol{Q}$ for $n > 1$ correlates to minimizing the spectrum of current harmonics – inclusive of grid voltage distortions. If the nth current harmonic begins to exceed a limit, its respective weighting in $\boldsymbol{Q}$ can simply be increased. By increasing the tracking error penalty for the nth harmonic, RT-OPP is more biased toward minimizing it.

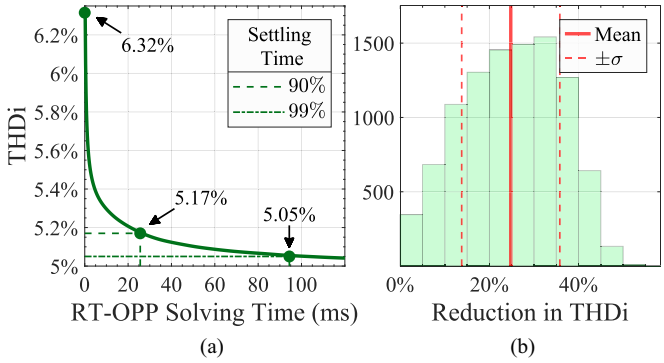

Fig. 8. Experimental Monte-Carlo results for 10,000 steps from an ideal to a randomly distorted grid voltage of RT-OPP performing HDM. (a) Average solving time of RT-OPP with respect to the THDi of an OPP from an LUT at $t = 0$ is shown by the solid green line. The settling time to a variety of values is given as per the legend. (b) Histogram of the data set is shown with the mean and a single standard deviation added.

TABLE III
RT-OPP EXECUTION TIMES

Objective	Min (μs)	Mean (μs)	Max (μs)
SHC	34.76	34.82	34.88
HDM	99.76	99.85	100.56

C. Execution Times

For the preceding results, the RT-OPP algorithm was executed at a rate of 5 kHz. The min, mean, and max execution times for SHC and HDM are given in Table III.

To investigate the computational burden of RT-OPP, the execution times in Table III are discussed and compared against incumbent NLP approaches for SHC and HDM.

1) SHC Using ANN-SQP: For SHC, ANN-SQP [23] is a promising strategy. However, before comparing execution times, the hardware platform used in their work must be examined. In [23], a powerful Intel i7 4.2 GHz quad core CPU yielded execution times within the range of 20 μs to 210 μ s. Compared to the 600 MHz microcontroller used in this work, that used in [23] is significantly more powerful. Despite this considerable difference in computing power, RT-OPP performs SHC in less than 35 μs.

A large variability in execution times of almost 200 μs for ANN-SQP diminishes the benefits of occasional fast executions—the sample rate is limited by the maximum execution time. Whereas for RT-OPP, by using an optimal analytic update policy (28) for optimization, precise execution times no more than 35 μ s and within 60 ns of the mean are yielded. Therefore, RT-OPP can be executed at more than five times the sample rate of ANN-SQP with comparably less computing power.

A final remark for ANN-SQP is a limited versatility. For each harmonic objective, a new ANN must be trained. This cumbersome task is in contrast to RT-OPP; a new harmonic objective can be tailored online by simply adjusting $\boldsymbol{Q}$.

2) HDM Using a Real-Time OPP Solver: Prior to this proposal, the authors explored computing an OPP to compensate for estimated grid voltage harmonics in real-time [22]. Compared to RT-OPP, a key difference is it performed global optimization, rather than local optimization. Therefore, it could yield larger

reductions in THDi at the expense of variable execution times within a few hundred milliseconds.

A limitation is it returned a single solution, so an additional stage to adjust the OPP during converter operation is required. As suggested earlier, RT-OPP can serve as a real-time companion to NLP solvers. It can adjust their more optimal pulse patterns in real-time while preserving their original harmonic objective.

V. Conclusion

The key contribution of this work is a new algorithm to optimize pulse patterns in real-time. The proposed RT-OPP leverages an optimal analytic update policy to sequentially adjust the switching angles to achieve a given harmonic objective. Unlike cumbersome NLP approaches, RT-OPP is of low computational burden and is feasible for implementation on a standard microcontroller at a high sample rate.

To verify the proposal's potential, a challenging case study of a grid-connected converter system operating with a distorted PCC voltage was explored. As supported by experimental results for two contrasting harmonic objectives, RT-OPP successfully compensates for a distorted grid voltage. For SHC, the grid voltage harmonics are rejected to eliminate the respective components from the converter's output current. Whereas for HDM, RT-OPP compensates for these grid voltage distortions to significantly improve harmonic performance. Unlike ANNs, the proposed RT-OPP requires a simple pulse pattern LUT that assumes nominal operating conditions. In addition, it is more versatile, as it was tailored for these different harmonic objectives by adjusting a single weighting matrix.

For future work, this versatility of RT-OPP affords it the potential to excel at other challenging applications. One example discussed is enforcing conformance to current harmonic limits, such as IEEE-519 [30]. Other potential endeavors could be exploring weak grids, penalizing commutations that occur at high currents to reduce switching losses or interfacing RT-OPP with more advanced pulse pattern controllers.

Appendix A
System Model Parameters

The parameters used to model the grid-connected converter system for the experimental results are given in Table IV. These system model parameters were originally from [37] and then streamlined from an *LC* to an *L* output filter in [22].

TABLE IV
System Model Parameters

Parameter	Symbol	SI Value	pu
Rated Apparent Power	S_B	9 MVA	1.0
Rated Voltage	V_B	3.15 kV	1.0
Rated Current	I_B	1.65 kA	1.0
Rated Frequency	f_1	50 Hz	1.0
DC-Link Voltage	V_{DC}	4.84 kV	1.53
Filter ESL	L_f	876 μH	0.25
Filter ESR	R_f	16.8 mΩ	0.018
Grid ESL	L_g	351 μH	0.1
Grid ESR	R_g	11 mΩ	0.025
Grid Voltage	V_g	3.15 kV	1.0

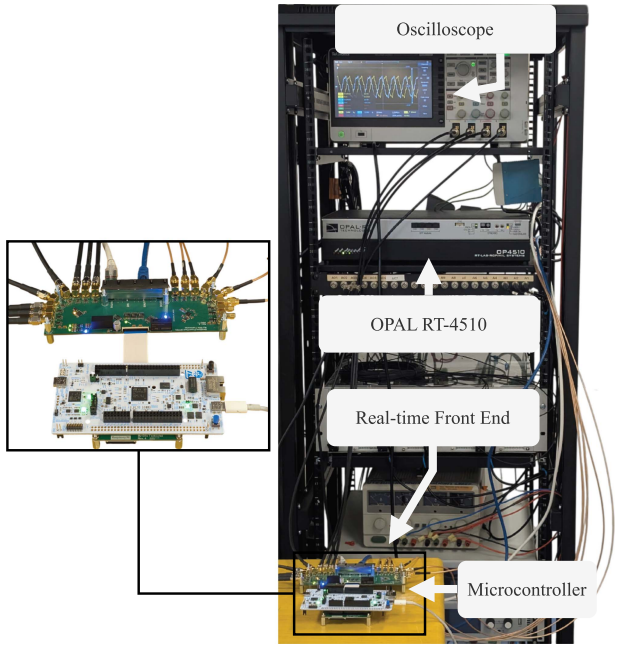

Fig. 9. Complete laboratory setup for the experimental results. A digital twin of the grid-connected converter system is modeled by the OPAL RT-4510 with the proposed RT-OPP implemented on a standard microcontroller.

Appendix B
Laboratory Setup

The complete laboratory setup used to acquire the experimental results is depicted in Fig. 9.

References

[1] N. Mohan, T. M. Undeland, and W. P. Robbins, *Power Electronics*. Hoboken, NJ, USA: Wiley, 2002.
[2] R. Teodorescu, M. Liserre, and P. Rodrıguez, *Grid Converters for Photovoltaic and Wind Power Systems*. Hoboken, NJ, USA: Wiley, Dec. 2010.
[3] D. Holmes and T. Lipo, *Pulse Width Modulation for Power Converters: Principles and Practice*. 1st ed. Hoboken, NJ, USA: Wiley, 2003.
[4] T. Geyer, *Model Predictive Control of High Power Converters and Industrial Drives*. Hoboken, NJ, USA: Wiley, 2017.
[5] H. S. Patel and R. G. Hoft, "Generalized techniques of harmonic elimination and voltage control in thyristor inverters: Part I–Harmonic elimination," *IEEE Trans. Ind. Appl.*, vol. IA-9, no. 3, pp. 310–317, May 1973.
[6] G. S. Buja, "Optimum output waveforms in PWM inverters," *IEEE Trans. Ind. Appl.*, vol. IA-16, no. 6, pp. 830–836, Nov. 1980.
[7] L. G. Franquelo, J. Napoles, R. C. P. Guisado, J. I. Leon, and M. A. Aguirre, "A flexible selective harmonic mitigation technique to meet grid codes in three-level PWM converters," *IEEE Trans. Ind. Electron.*, vol. 54, no. 6, pp. 3022–3029, Dec. 2007.
[8] C. Buccella, C. Cecati, M. G. Cimoroni, and K. Razi, "Analytical method for pattern generation in five-level cascaded H-bridge inverter using selective harmonic elimination," *IEEE Trans. Ind. Electron.*, vol. 61, no. 11, pp. 5811–5819, Nov. 2014.
[9] M. S. A. Dahidah, G. Konstantinou, and V. G. Agelidis, "A review of multilevel selective harmonic elimination PWM: Formulations, solving algorithms, implementation and applications," *IEEE Trans. Power Electron.*, vol. 30, no. 8, pp. 4091–4106, Aug. 2015.
[10] C. Wang, Q. Zhang, W. Yu, and K. Yang, "A comprehensive review of solving selective harmonic elimination problem with algebraic algorithms," *IEEE Trans. Power Electron.*, vol. 39, no. 1, pp. 850–868, Jan. 2024.
[11] J. Nocedal, and S. Wright, *Numerical Optimization,* (Springer Series in Operations Research and Financial Engineering). New York: Springer, 2006.
[12] A. Birth, T. Geyer, H. D. T. Mouton, and M. Dorfling, "Generalized three-level optimal pulse patterns with lower harmonic distortion," *IEEE Trans. Power Electron.*, vol. 35, no. 6, pp. 5741–5752, Jun. 2020.

[13] I. Koukoula, P. Karamanakos, and T. Geyer, "Loss-constrained optimized pulse patterns for three-level converters with robustness to power factor variations," in *Proc. IEEE Energy Convers. Congr. Expo.*, Oct. 2023, pp. 4644–4651.
[14] S. Rahmanpour, P. Karamanakos, and T. Geyer, "Three-level optimized pulse patterns for grid-connected converters with LCL filters," in *Proc. IEEE Energy Convers. Congr. Expo.*, 2023, pp. 1430–1437.
[15] T. Dorfling and T. Geyer, "Thermally constrained optimized pulse patterns for medium-voltage neutral-point-clamped converters," *IEEE Trans. Power Electron.*, vol. 39, no. 10, pp. 13160–13176, Oct. 2024.
[16] T. Geyer, P. Karamanakos, and I. Koukoula, "Optimized pulse patterns with bounded semiconductor losses," *IEEE Trans. Power Electron.*, vol. 39, no. 3, pp. 3233–3243, Mar. 2024.
[17] Z. Zhang, G. Chen, and D. Xu, "Harmonic programmed modulation for high-power medium voltage energy conversion: Formulation, solving approach, and implementation," *IEEE Trans. Power Electron.*, vol. 40, no. 6, pp. 7872–7892, Jun. 2025.
[18] J. David, S. Elphick, and D. Robinson, "Management of harmonic distortion for large renewable energy generation," in *Proc. 32nd Australas. Universities Power Eng. Conf.*, Sep. 2022, pp. 1–6.
[19] S. Rahmanpour, P. Karamanakos, and T. Geyer, "Optimized pulse patterns for converters connected to a distorted grid via LCL filters," in *Proc. Energy Convers. Congr. Expo. Europe*, 2024, pp. 1–8.
[20] J. David, D. Robinson, and S. Elphick, "Aggregation of multiple inverter-based harmonic sources within a renewable energy generation plant," in *Proc. 20th Int. Conf. Harmon. Qual. Power*, May 2022, pp. 1–6.
[21] H. Zhou, Y. W. Li, N. R. Zargari, Z. Cheng, R. Ni, and Y. Zhang, "Selective harmonic compensation (SHC) PWM for grid-interfacing high-power converters," *IEEE Trans. Power Electron.*, vol. 29, no. 3, pp. 1118–1127, Mar. 2014.
[22] E. Tsekouras, R. P. Aguilera, and T. Geyer, "Real-time computation of optimized pulse patterns for compensation of estimated grid voltage harmonics," in *Proc. IEEE Energy Convers. Congr. Expo.*, Oct. 2024, pp. 4590–4597.
[23] I. Ibanez-Hidalgo et al., "Real time selective harmonic control—PWM based on ANNs," *IEEE Trans. Power Electron.*, vol. 39, no. 1, pp. 768–783, Jan. 2024.
[24] I. Ibanez-Hidalgo et al., "Enhanced PI control based SHC-PWM strategy for active power filters," *IEEE Open J. Ind. Electron. Soc.*, vol. 5, pp. 1174–1189, 2024.
[25] F. Blaabjerg, ed., *Control of Power Electronic Converters and Systems: Volume 1*. vol. 1, 1st ed. Cambridge, MA, USA: Academic Press, Jan. 2018.
[26] H. Zhao, T. Jin, S. Wang, and L. Sun, "A real-time selective harmonic elimination based on a transient-free inner closed-loop control for cascaded multilevel inverters," *IEEE Trans. Power Electron.*, vol. 31, no. 2, pp. 1000–1014, Feb. 2016.
[27] M. Ahmed, A. Sheir, and M. Orabi, "Real-time solution and implementation of selective harmonic elimination of seven-level multilevel inverter," *IEEE Trans. Emerg. Sel. Topics Power Electron.*, vol. 5, no. 4, pp. 1700–1709, Dec. 2017.
[28] K. Yang et al., "Real-time switching angle computation for selective harmonic control," *IEEE Trans. Power Electron.*, vol. 34, no. 8, pp. 8201–8212, Aug. 2019.
[29] C. Buccella et al., "Recursive selective harmonic elimination for multilevel inverters: Mathematical formulation and experimental validation," *IEEE Trans. Emerg. Sel. Topics Power Electron.*, vol. 11, no. 2, pp. 2178–2189, Apr. 2023.
[30] *IEEE Standard for Harmonic Control in Electric Power Systems*, IEEE Std 519-2022 (Revision of IEEE Std 519-2014), pp. 1–31, 2022.
[31] R. Cardoso, R. F. de Camargo, H. Pinheiro, and H. A. Gründling, "Kalman filter based synchronization methods," in *Proc. 37th IEEE Power Electron. Specialists Conf.*, Jun. 2006, pp. 1–7.
[32] K. Kennedy, G. Lightbody, and R. Yacamini, "Power system harmonic analysis using the Kalman filter," in *Proc. IEEE Power Eng. Soc. Gen. Meeting (IEEE Cat. No.03CH37491)*, 2003, vol. 2, pp. 752–757.
[33] C. Fischer, S. Mariéthoz, and M. Morari, "A model predictive control approach to reducing low order harmonics in grid inverters with LCL filters," in *Proc. 39th Annu. Conf. IEEE Ind. Electron. Soc.*, 2013, pp. 3252–3257.
[34] J. M. Kanieski, R. Cardoso, H. Pinheiro, and H. A. Grundling, "Kalman filter-based control system for power quality conditioning devices," *IEEE Trans. Ind. Electron.*, vol. 60, no. 11, pp. 5214–5227, Nov. 2013.
[35] G. C. Goodwin, S. F. Graebe, and M. E. Salgado, *Control System Design*. India: Pearson India Education, 2016.
[36] S. Vazquez, E. Zafra, R. P. Aguilera, T. Geyer, J. I. Leon, and L. G. Franquelo, "Prediction model with harmonic load current components for FCS-MPC of an uninterruptible power supply," *IEEE Trans. Power Electron.*, vol. 37, no. 1, pp. 322–331, Jan. 2022.
[37] T. Dorfling, H. d. T. Mouton, and T. Geyer, "Generalized model predictive pulse pattern control based on small-signal modeling—Part 2: Implementation and analysis," *IEEE Trans. Power Electron.*, vol. 37, no. 9, pp. 10488–10498, Sep. 2022.

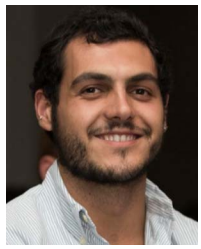

Ellis Tsekouras (Graduate Student Member, IEEE) received the certificate III, diploma, and advanced diploma in electrotechnology from TAFE NSW Australia, in 2013, 2014, and 2015, respectively, the B.Eng. (*Hons.*) degree in electrical engineering from University of Technology Sydney, Ultimo, Australia, in 2021, and was awarded the University Medal, where he has been working toward the Ph.D degree in electrical engineering, since 2023. Outside of academia, he is a Senior Electrical Engineer with Resmed and designs motor drive control systems for sleep and respiratory care medical devices. His research interests are focused on model predictive control and optimized pulse patterns for power converters.

Mr. Tsekourasas was a recipient of their Research Excellence scholarship.

Ricardo P Aguilera (Member, IEEE) received the B.Sc. degree in electrical engineering from the Universidad de Antofagasta, Antofagasta, Chile, in 2003, the M.Sc. degree in electronics engineering from the Universidad Tecnica Federico Santa Maria, Valparaíso, Chile, in 2007, and the Ph.D. degree in electrical engineering from The University of Newcastle (UoN), Newcastle, NSW, Australia, in 2012.

From 2012 to 2013, he was a Research Academic with UoN, where he was a part of the Centre for Complex Dynamic Systems and Control. From 2014 to 2016, he was a Senior Research Associate with The University of New South Wales, Sydney, NSW, Australia, where he was a part of the Australian Energy Research Institute. Since 2016, he has been with the School of Electrical and Data Engineering, University of Technology Sydney, Sydney, where he currently holds an Associate Professor position. His research interests include theoretical and practical aspects on model predictive control with application to power electronics, renewable energy integration, and microgrids.

Tobias Geyer (Fellow, IEEE) received the Dipl.- Ing. degree in electrical engineering, the Ph.D. degree in control engineering, and the Habilitation degree in power electronics al from ETH Zurich, Zurich, Switzerland, in 2000, 2005, and 2017, respectively.

After his Ph.D., he spent three years with GE Global Research, Munich, Germany, three years with the University of Auckland, Auckland, New Zealand, and eight years with ABB's Corporate Research Centre, Baden-Dättwil, Switzerland. In 2020, he joined ABB's Medium-Voltage Drive division as R&D Platform Manager of the ACS6080. In 2022, he became a Corporate Executive Engineer. He has been an extraordinary Professor with Stellenbosch University, Stellenbosch, South Africa, since 2017. He is the author of more than 40 patent families, 160 publications, and the book Model Predictive Control of High Power Converters and Industrial Drives (Wiley, 2016). He teaches a regular course on model predictive control with ETH Zurich. His research interests include medium-voltage and low-voltage drives, utility-scale power converters, optimized pulse patterns and model predictive control.

Dr. Geyer was the recipient of the IEEEPELS Modeling and Control Technical Achievement Award in 2022, the Semikron Innovation Award in 2021, and the Nagamori Award in 2021. He was also the recipient of two Prize Paper Awards of IEEE Transactions and three Prize Paper Awards at IEEE conferences. He is a former Associate Editor of IEEE TRANSACTIONS ON INDUSTRY APPLICATIONS (from 2011 until 2014) and IEEE TRANSACTIONS ON POWER ELECTRONICS (from 2013 until 2019). He was an International Program Committee Vice Chair of the IFAC conference on Nonlinear Model Predictive Control inMadison, WI, USA, in 2018. He was a Distinguished Lecturer of the IEEE Power Electronics Society from 2020 to 2023.